Raman scattering of intense, short laser pulses in modulated plasmas

J. P. Palastro, T. M. Antonsen Jr., A. Pearson, W. Zhu, and N. Jain
Institute for Research in Electronics and Applied Physics, University of Maryland, College Park, Maryland 20740, USA
(Received 20 December 2010; published 28 April 2011)

We examine the exponentiation of the Raman forward scattering instability in modulated plasma channels computationally and analytically. An evolution equation for the complex phases of the Raman scattered waves treating the spatial localization and discrete nature of the channel modes is derived. Simulations with WAKE [P. Mora and T. M. Antonsen Jr., Phys. Plasmas **4**, 217 (1997).] verify the theory in the linear growth regime and provide insight into the nonlinear stage of the instability when cascading and pump depletion play a role. We find that the exponentiation in modulated channels depends on two factors: the increase in coupling due to the increased plasma wavenumber in the high-density regions of the channel and a decreased coupling due to the reduced longitudinal spatial coherence. For the parameters considered, simulations show that the finite extent of the pump pulse is more significant in determining the exponentiation than phase mixing due to the transverse variation of the channel. Both the theory and simulations confirm that modulated channels allow for the stable guiding of longer pulses than nonmodulated channels.

DOI: 10.1103/PhysRevE.83.046410 PACS number(s): 52.38.Bv, 42.65.Tg, 41.75.Jv

I. INTRODUCTION

The stimulated Raman forward scattering instability occurs when an incident laser pulse scatters from plasma density fluctuations. The resulting scattered electromagnetic waves are downshifted (Stokes) and upshifted (anti-Stokes) by the plasma frequency. The ponderomotive force resulting from the beating of the scattered waves with the incident wave reinforces the density fluctuations, driving plasma waves of ever increasing amplitude [1–3]. As the sidebands grow in amplitude, they themselves undergo the instability, and the feedback process continues until the wave energy is distributed in the spectral domain or cascading [3] or another nonlinear process takes over [4].

Prior to the development of lasers producing pulse durations on the order of the plasma period for typical gas jets, the self-modulation instability [5] and forward Raman scattering were the predominant method for producing plasma wakefields: the self-modulated wakefield regime [6–8]. Traditionally, the two instabilities were distinguished by the transport of laser pulse energy [5]. In self-modulation, pulse energy is transferred radially, while in Raman scattering the transfer is axial. In our analysis, we label both axial and transverse transfer as Raman scattering. The electrons trapped in the standing density waves (wakefields) resulting from the instabilities follow the phase fronts and can be accelerated to several hundred MeV in only several centimeters [9–11]. The promise of application led to several experiments and analytic results describing Raman forward scattering and self-modulation, but the analysis was primarily focused on uniform background plasmas in the lab frame [12–16].

Almost simultaneously with the development of self-modulated wakefields was the development of miniature plasma-guiding structures or channels [17–19]. The channels, produced by hydrodynamic expansion of a heated column of plasma, provide a transversely varying dielectric constant that is smaller on the edges than in the center combating the natural transverse expansion of the laser due to diffraction. The prospect that plasma channels could guide pulses over many gain lengths (exponentiations of the instability) led to interest in how the Raman instability may evolve in a channel [20–30]. In particular, Shvets *et al*. showed that the transverse variation of the structure leads to phase mixing, causing the instability to evolve at a reduced growth rate compared to transversely uniform plasmas [19,20]. In addition to investigations considering the transverse variation in the plasma density, density variations from channel tapers were also explored [31].

Even before the advent of plasma channels and the self-modulated wakefield regime, modulated plasmas have been of interest [32–35]. In early investigations modulated plasmas were considered in primarily two scenarios: beat wave excitation by two pump laser pulses detuned by the plasma frequency and plasma wavenumber [34,35] or by stimulated Brillouin waves in the plasma [33]. Figueroa *et al*. investigated the general properties of wave propagation in density-modulated plasmas including the effects of slow-wave dispersion and forbidden frequency regions corresponding to band gaps [32]. In the case of electron plasma waves co-localized with a modulated Brillouin perturbation, Figueroa demonstrated that the slow-wave dispersion of plasma waves predicted real frequency shifts altering the phase matching of Raman scattering [33].

The creation of modulated plasma channels by Layer *et al*. expanded the applicability of plasma channels, allowing for quasiphase matching to THz radiation and relativistic electron beams over many diffraction lengths [36–40]. For quasiphase-matched acceleration of electrons, the periodic structure of the plasma channel results in a guided pulse composed of several spatial harmonics. While the central harmonic of the laser pulse has a phase velocity greater than the speed of light in vacuum, individual spatial harmonics can have subluminal phase velocities. The subluminal phase velocities allow for phase matching with relativistic electrons, accelerating the electrons to high energies. Because the group velocity of the pulse is less than the speed of mildly relativistic electrons, for long enough plasma channels, the energy gain of quasiphase-matched direct acceleration is limited by the time it takes an electron to outrun the laser pulse. This

makes the Raman forward scattering instability of particular interest. As the pulse length is increased, the energy gain in quasiphase-matched direct acceleration increases, but the pulse also becomes more susceptible to instability. If the gain of the instability is too large, the pulse quality can be diminished, and the accelerating field spoiled.

Here we examine the evolution of the Raman scattering instability in modulated plasma channels analytically and computationally. Starting from Maxwell's equations, an evolution equation for the complex phase is derived that is capable of modeling uniform, axially varying, and radially varying background plasmas. The equation provides instability growth rates in both the spatiotemporal regime where the instability exponentiation depends on the pulse frame coordinate [41] and in a standard long-pulse regime. Simulations with WAKE [42] are used to verify the theory and examine the instability in the nonlinear regime where pump depletion and cascading play a role. While transverse phase mixing in channels has been described analytically by Shvets *et al*. [21,22], we find that with significant phase mixing the instability behaves as though it is strongly damped, resulting in different growth rates than those predicted in the reference. In addition, we find that for the parameters considered here, the transverse phase mixing plays little role in the exponentiation of the instability. The finite duration of the laser pulse has the dominant effect on the instability growth rates. While density-modulated plasmas have been investigated by Figueroa *et al*., predictions of growth rates and a systematic investigation of the Raman forward scattering instability were not considered. Detailed simulations of the forward instability in channels with correspondence to theory and descriptions of the loss of spatial coherence due to axial modulations are absent in the literature. In particular, we find that density modulations lead to a reduction in growth rates associated with the Raman forward instability.

This paper is organized as follows. In Sec. II we detail the laser pulse and plasma wave evolution equations and present the background density profile. The pump laser pulse dispersion and phase evolution is derived in Sec. III. Sec. IV contains the derivation of the equation describing the complex phase evolution of the scattered electromagnetic wave in Raman forward scattering. In Sec. V we obtain analytic results in a variety of situations including transversely uniform and channeled plasmas. Sec. VI presents simulation results using WAKE and verification of the results of Sec. V. Sec. VII gives the summary and conclusions.

II. LASER PULSE AND PLASMA WAVE EQUATIONS

We begin by separating the fields into high-frequency (near the laser frequency) and low-frequency (near the plasma frequency) components. Our analysis will assume tenuous plasma such that the laser frequency is much greater than the plasma frequency.

Under the separation of timescales, the normalized vector potential $\vec{a} = e\vec{A}/m_e c^2$ satisfies the wave equation

$$\left[c^2\nabla\times\left(\nabla\times\vec{a}\right)+\frac{\partial^2\vec{a}}{\partial t^2}\right] = -\omega_p^2(r,z)\left[1+\frac{\delta n}{n}-\frac{1}{2}\langle|\vec{a}|^2\rangle\right]\vec{a} \tag{1}$$

in the weakly relativistic limit. Here $\vec{a}$ is the vector potential in a gauge where the electrostatic potential $\phi = 0$, e is the fundamental unit of charge, m_e is the electron mass, and c is the speed of light. The right-hand side of Eq. (1) represents the high-frequency plasma current. Here $\omega_p^2(r,z) = 4\pi e^2 n(r,z)/m_e$ is the spatially dependent plasma frequency, and $n(r,z)$ is the ambient electron density. The quantity δn is the low-frequency perturbed electron density, which will be derived subsequently. The angular bracket indicates a time average of a high-frequency field. This term represents the relativistic correction to the plasma current.

The background (equilibrium) electron density profile is chosen to model the experimentally produced corrugated plasma waveguides [36] paralleling our previous studies:

$$\omega_p^2(r,z) = \omega_{p,0}^2[1+\delta\sin(k_m z)] + \omega''^2_{p,0} r^2/2. \tag{2}$$

Throughout the text, we will use the plasma wavevector and frequency interchangeably through the relations $k_p^2(r,z) = \omega_p^2(r,z)/c^2$, $k_{p,z}^2 = \omega_{p,z}^2/c^2 = \omega_p^2(0,z)/c^2$, and $k_{p,r}^2 = \omega_{p,r}^2/c^2 = \omega_p^2(r,0)/c^2$.

The low-frequency response of the plasma is driven by the ponderomotive potential of the laser field

$$V_p = \tfrac{1}{2} m_e c^2 \langle|\vec{a}|^2\rangle. \tag{3}$$

We assume the plasma responds linearly to the ponderomotive force. For the parameters considered here, the radial dependence of the ambient electron density is weak such that $\omega_{p,0}^2 \gg \frac{1}{2}\omega''^2_{p,0} r^2$ for values of r where the laser pulse amplitude is large (roughly the spot size). As a consequence, the plasma wave is electrostatic. We can then write the frequency domain electrostatic potential as the solution of Poisson's equation,

$$\nabla\cdot(1+\chi_e)\nabla e\bar{V}_e = \nabla\cdot\chi_e\nabla\bar{V}_p, \tag{4}$$

where the overbar indicates the quantity is expressed in the frequency domain, and $\chi_e = -\omega_p^2(r,z)/\omega^2$ is the plasma susceptibility at frequency ω. The density perturbation then follows from the electrostatic potential through Poisson's equation,

$$\delta n = \frac{1}{4\pi e}\nabla^2 V_e, \tag{5}$$

which is valid in both the time and frequency domain. The density perturbation is inserted into Eq. (1), completing the system of governing equations.

III. PUMP LASER PULSE PROPAGATION

We start by writing the vector potential of a single radial eigenmode, pump electromagnetic pulse propagating along the z axis as follows:

$$\vec{a}_0(\vec{x},t) = \hat{\vec{a}}_0(\vec{x}_\perp, z - c_{g,0}t, z)e^{i(\hat{k}_0 z-\omega_0 t)} + \text{c.c.}, \tag{6}$$

where $\hat{k}_0 \equiv \omega_0/c$ and ω_0 provide the rapidly varying components of the phase. The group velocity can be expressed as $c_{g,0} = c^2 k_0/\omega_0$, and k_0 will be determined subsequently. The envelope function $\hat{\vec{a}}_0$ contains the temporal pulse shape through the variable $z - c_{g,0}t$, the slow-varying axial phase through z, and the transverse variation through $\vec{x}_\perp$. The

wavevector $\hat{k}_0$ is taken to be greater than any other spatial variation in Eq. (6): $\hat{k}_0 \gg \partial_z \ln(a_0)$. Similarly for the frequency: $\omega_0 \gg \partial_t \ln(a_0)$.

Inserting Eq. (6) into Eq. (1) and dropping slowly varying terms in z and t (second-order derivatives) we obtain the familiar nonlinear Schrödinger equation for the pump laser's vector potential:

$$\left[2i\hat{k}_0\frac{\partial}{\partial z}+\nabla_\perp^2\right]\hat{\vec{a}}_0 = k_p^2(r,z)\left[1+\frac{\delta n}{n}-\frac{1}{2}\langle|\hat{\vec{a}}_0|^2\rangle\right]\hat{\vec{a}}_0, \tag{7}$$

where we performed the variable transformation $\xi = z - c_{g,0}t$, $z' = z$, and renamed z' as z. In Eq. (7), $\delta n/n$ evolves in ξ according to the inverse Fourier transform of Eqs. (4) and (5). We note that including the group velocity $c_{g,0}$ instead of the speed of light in a vacuum in Eq. (7) is consistent with our approximation to drop second-order derivatives.

We now remove an additional phase from $\hat{\vec{a}}_0$ and separate the group velocity propagation from the transverse variation as follows:

$$\hat{\vec{a}}_0(\vec{x},\xi,z) = \alpha_0(\xi)\vec{u}_0(\vec{x}_\perp)e^{i\phi_0(\xi,z)}, \tag{8}$$

where α_0 is the amplitude of $\vec{a}_0$ and $\vec{u}_0(\vec{x}_\perp)$ corresponds to an eigenmode of the channel, which we choose to be the lowest. Here we consider radially polarized modes, which are of more direct interest as discussed in Refs. [37] and [38]. The dispersion of linearly polarized modes will be different by a numerical factor in the diffractive contribution and instability growth rates. For a parabolic density profile, the eigenmodes of the radial component of the vector potential in the structure are given by $\vec{u}_n(r) = u_{rn}(r)\hat{r} + u_{zn}(r)\hat{z}$, where $u_{rn}(r) = x^{1/2}L_n^1(2x)e^{-x}/\sqrt{n+1}$ and $u_{zn}(r) = i(k_0 r)^{-1}\partial_r(r u_{rn})$. Here n is an integer, $x = r^2/w_{ch}^2$, and the functions L_n^1 represent the associated Laguerre polynomials, and $w_{ch} = (2c)^{1/2}(2/\omega''^2_{p,0})^{1/4}$. The eigenmodes satisfy the equation

$$\left[\frac{1}{r}\frac{\partial}{\partial r}r\frac{\partial}{\partial r}-\frac{1}{r^2}-\frac{4r^2}{w_{ch}^4}\right]u_{rn} = -k_{\perp,\ell}^2 u_{rn}, \tag{9}$$

where the eigenvalue is given by $k_{\perp,n}^2 = 8(n+1)/w_{ch}^2$. In order that the pump field can be represented as a single radial eigenfunction it is necessary that the plasma density perturbation, $\delta n/n$, and the relativistic correction, $\langle|\vec{a}|^2\rangle$, be sufficiently small. Basically we require that these terms are small when compared with the spacing between adjacent eigenvalues. Specifically we assume $(k_{p,0}w_{ch})^{-2} > \frac{1}{16}a_0^2$. Here we are considering only variation of the pulse in radial and axial coordinates; thus hosing-type instabilities of the laser pulse will not be considered [43].

Inserting Eq. (8) into Eq. (7), projecting onto $\hat{\vec{a}}_0^*$ and integrating over the cross-sectional area, we obtain an equation for the local shift of the pump pulse's wavenumber $\partial_z\phi_0$:

$$\frac{\partial}{\partial z}\phi_0 = -\kappa_0(z) - \delta\kappa_0(\xi,z), \tag{10}$$

where

$$\kappa_0(z) = \frac{1}{2}\frac{k_{p,z}^2 + k_{\perp,0}^2}{\hat{k}_0} \tag{11}$$

is the linear wavenumber shift due to the plasma and presence of the channel, and

$$\delta\kappa_0(\xi,z) = -\frac{1}{4}\alpha_0^2(\xi)\left[\frac{I_0^{nl}k_{p,z}^2 + I_0^{nl,ch}k_{\perp,0}^2}{\hat{k}_0}\right] \tag{12}$$

is the shift resulting from the relativistic reduction in the plasma frequency. For the parameters considered here, the relativistic shift to the plasma frequency is small, and ϕ_0 is predominantly a function of z. In Eq. (12) we have defined the following transverse overlap integrals:

$$I_j^{nl} = \frac{2}{A_j}\int|\vec{u}_j|^2|\vec{u}_0|^2 d^2r, \tag{13a}$$

$$I_j^{nl,ch} = \frac{1}{w_{ch}^2 A_j}\int|\vec{u}_j|^2|\vec{u}_0|^2 r^2 d^2r, \tag{13b}$$

where $A_j = \int|\vec{u}_j|^2 d^2r$ is the intensity weighed area of the mode. The subscript j is left ambiguous because the scattered light wave will have overlap integrals of the same form when we consider the nonlinear dispersion relation in the next section. The integrals represent the numerical factors for the relativistic nonlinear (*nl*) shift to the plasma frequency and the nonlinear shift to the profile's diffractive contribution (*nl, ch*). Evaluating the integrals given by Eqs. (13a) and (13b), and inserting them in Eq. (12), we obtain for the total wavenumber $k_0 = \hat{k}_0 + \partial_z\phi_0$

$$k_0 = \hat{k}_0 - \frac{1}{2}\frac{k_{p,z}^2}{\hat{k}_0}\left[1-\frac{1}{8}\alpha_0^2(\xi)\right] - \frac{1}{2}\frac{k_{\perp,0}^2}{\hat{k}_0}\left[1-\frac{3}{64}\alpha_0^2(\xi)\right]. \tag{14}$$

Every term appearing in Eq. (10) is strictly real, and thus $\phi_0 = \phi_0^*$ and $k_0 = k_0^*$.

The local dispersion relation expresses the wavenumber as a periodic function of distance with period equal to that of the density modulations. The local dispersion relation can complicate phase matching in a three-wave process as wavenumbers vary from point to point in the channel. In fact, the nonstationary position of the phase is what will end up reducing the growth rate. Here we note that the pump wave can be expressed as a sum of spatial harmonics with constant wavenumbers:

$$\hat{\vec{a}}_0(\vec{x},\xi,z) = \alpha_0(\xi)\vec{u}_0(\vec{x}_\perp)\sum_\ell i^\ell J_\ell(\psi)e^{i\phi_{0,\ell}}, \tag{15}$$

where J_ℓ is the ℓth Bessel function, $\psi = \delta\omega_{p,0}^2(1-\frac{1}{8}\alpha_0^2)/c^2k_m\hat{k}_0$, and there are now an infinite number of phases for the pump laser satisfying the equation

$$\frac{\partial}{\partial z}\phi_{0,\ell} = -\kappa_{0,\ell} - \delta\kappa_{0,\ell}, \tag{16}$$

where

$$\kappa_{0,\ell} = \frac{1}{2}\frac{k_{p,0}^2 + k_{\perp,0}^2}{\hat{k}_0} - \ell k_m \tag{17}$$

is the linear wavenumber shift due to the plasma and presence of the channel, and

$$\delta\kappa_0(\xi) = -\frac{1}{4}\alpha_0^2(\xi)\left(\frac{I_0^{nl}k_{p,0}^2 + I_0^{nl,ch}k_{\perp,0}^2}{\hat{k}_0}\right). \tag{18}$$

The nonlocal dispersion relation for each spatial harmonic is then

$$k_{0,\ell} = \hat{k}_0 + \ell k_m - \frac{1}{2}\left[1 - \frac{1}{8}\alpha_0^2(\xi)\right]\frac{k_{p,0}^2}{\hat{k}_0} - \left[1 - \frac{3}{64}\alpha_0^2(\xi)\right]\frac{k_{\perp,0}^2}{\hat{k}_0}. \quad (19)$$

While this formalism is useful for phase matching to relativistic electron beams, as in Ref. [37], for the remainder of this text, we focus on the local dispersion.

IV. NONLINEAR EVOLUTION

We now consider the growth of the Raman forward scattering instability. The scattering of the pump pulse from density fluctuations in the plasma results in electromagnetic sidebands. The total vector potential including the sidebands can be expressed as follows:

$$\vec{a}(\vec{x},t) = \hat{\vec{a}}_0(\vec{x}_\perp,\xi,z)e^{i(\hat{k}_0 z - \omega_0 t)} + \sum_\pm \hat{\vec{a}}_\pm(\vec{x}_\perp,\xi,z)e^{i(\hat{k}_\pm z - \hat{\omega}_\pm t)} + \text{c.c.}, \quad (20)$$

where we write for the sidebands

$$\hat{\vec{a}}_\pm(\vec{x},\xi,z) = \alpha_\pm \vec{u}_\pm(\vec{x}_\perp)e^{i\phi_\pm(\xi,z)}. \quad (21)$$

Each sideband is in a superposition of eigenmodes of the channel, which may be different from the pump (assumed to be in the $n = 0$ mode). To lowest order, however, each scattered eigenmode of the sideband evolves independently. Furthermore, crosscoupling between sidebands is only available to identical eigenmodes. As a result, we can drop the indicator n on each eigenmode, set $\vec{u}_\pm = \vec{u}$, and consider them independently as in Eq. (21). The wavenumber and frequency for an eigenmode of the sidebands is given by

$$k_\pm = \hat{k}_\pm + \frac{\partial}{\partial z}\phi_\pm, \quad (22a)$$

$$\omega_\pm = \hat{\omega}_\pm - \frac{\partial}{\partial t}\phi_\pm, \quad (22b)$$

where the phases $\phi_\pm$ of the scattered waves are complex quantities whose imaginary parts will determine the growth of the instability. We choose to assign the spatial and temporal growth to the phase, rather than a complex amplitude, as it allows us to more easily calculate the time and space dependence of the growing modes. In this regard the quantities $\alpha_\pm$ are constants fixed at the initial seed levels of the sideband eigenmodes. One consequence of this treatment is that the absence of phase matching will result in an oscillatory $\phi_\pm$, making the connection between stationary phase and phase matching clear. In Appendix A we show that the complex phase is directly involved in action conservation. In particular Eq. (A4) shows that it is the real component of the phase that leads to a *direct proportionality* with the action, while the imaginary component describes transfer of action between waves.

Using Eqs. (20) and (22) we can evaluate the time average of $|\vec{a}|$ as

$$\tfrac{1}{2}\langle|\vec{a}|^2\rangle = |\hat{\vec{a}}_0|^2 + [(\hat{\vec{a}}_0^* \cdot \hat{\vec{a}}_+ + \vec{a}_0 \cdot \hat{\vec{a}}_-^*)e^{i(\hat{k}_e z - \hat{\omega}_e t)} + \text{c.c.}], \quad (23)$$

where $\hat{k}_e = \hat{k}_+ - \hat{k}_0 = \hat{k}_0 - \hat{k}_-^*$ and $\hat{\omega}_e = \hat{\omega}_+ - \omega_0 = \omega_0 - \hat{\omega}_-^*$ are the wavenumber and frequency of the low-frequency plasma wave excitations. We note that the time dependence of the ponderomotive potential will be determined by both the lowest order frequency (linear plasma frequency) $\hat{\omega}_e$ and the complex phase $\phi_\pm$. In this regard, the effective frequencies of the ponderomotive potential are

$$\omega_{e,\pm} = \hat{\omega}_e - \frac{\partial}{\partial t}\phi_\pm. \quad (24)$$

These will be the frequencies of the plasma wave excited by the ponderomotive potential associated with each of the sidebands.

The perturbed ponderomotive potential drives a density perturbation, which we write as follows:

$$\delta n(r,z,t) = \delta\hat{n}(r,z,t)e^{i(\hat{k}_e z - \hat{\omega}_e t)}. \quad (25)$$

The amplitude $\delta\hat{n}$ is obtained from Eqs. (4) and (5). We consider two limits of Eq. (4): when the longitudinal and transverse components of the Laplacian dominate. If the longitudinal component dominates, we have $e\bar{V}_e = [\chi_e/(1+\chi_e)]\bar{V}_p$ and $\nabla^2 e\bar{V}_e \simeq \nabla\cdot[\chi_e/(1+\chi_e)]\nabla\bar{V}_p$. On the other hand, if the transverse component dominates, $\nabla e\bar{V}_e = [\chi_e/(1+\chi_e)]\nabla\bar{V}_p$ and $\nabla^2 e\bar{V}_e \simeq \nabla\cdot[\chi_e/(1+\chi_e)]\nabla\bar{V}_p$. Thus an expression for the density that is correct in both limits is

$$\overline{\delta n} = \frac{1}{4\pi e^2}\nabla\cdot\left[\frac{\chi_e}{1+\chi_e}\right]\nabla\overline{V}_p. \quad (26)$$

We then Fourier invert Eq. (26) to find an expression for δn:

$$\frac{\delta n}{n} = \frac{1}{2\pi k_p^2}\nabla\cdot\sum_\pm\int dk\,\frac{\chi_e}{1+\chi_e}e^{-ik\xi}\nabla\bar{V}_{p,\pm}(k,r,z), \quad (27)$$

where

$$\bar{V}_{p,+}(k,r,z) = \alpha_+(\vec{u}\cdot\vec{u}_0^*)\int d\xi'\alpha_0(\xi')e^{i(k+\hat{k}_e)\xi' - i(\phi_0-\phi_+)} + \text{c.c.} \quad (28a)$$

$$\bar{V}_{p,-}(k,r,z) = \alpha_-(\vec{u}^*\cdot\vec{u}_0)\int d\xi'\alpha_0(\xi')e^{i(k+\hat{k}_e)\xi' + i(\phi_0-\phi_-^*)} + \text{c.c.} \quad (28b)$$

are the components of the ponderomotive potential and $\phi_a = \phi_a(\xi',z)$.

We now substitute the side bands into the wave equation [Eq. (1)] and project the equation onto the relevant transverse mode of the channel. We obtain the following pair of equations for the coupled side bands:

$$\left[\left(\frac{\omega_+}{c}\right)^2 - k_+^2 - 2(\kappa_+ + \delta\kappa_+)\hat{k}_+\right]\alpha_+ = \alpha_0 A^{-1}\int k_p^2\left[(\vec{u}_0\cdot\vec{u}^*)e^{i(\phi_0-\phi_+)}\frac{\delta\hat{n}}{n} - \alpha_0\alpha_-^*\left|\vec{u}_0^*\cdot\vec{u}\right|^2 e^{-i(\phi_+-\phi_-^*)}\right]d^2r \quad (29a)$$

and

$$\left[\left(\frac{\omega_-^*}{c}\right)^2-(k_-^*)^2-2(\kappa_++\delta\kappa_+)\hat{k}_-\right]\alpha_-^*=\alpha_0A^{-1}\int k_p^2\left[(\vec{u}_0^*\cdot\vec{u})e^{-i(\phi_0-\phi_-^*)}\frac{\delta\hat{n}}{n}-\alpha_0\alpha_+|\vec{u}_0^*\cdot\vec{u}|^2e^{-i(\phi_+-\phi_-^*)}\right]d^2r, \tag{29b}$$

where we have dropped second-order derivatives of the complex phases. For small pump amplitudes, the nonlinear phase shifts, $\delta\kappa_j$, and the second term under the integral can be dropped. In a plasma channel, the electromagnetic waves always have a perpendicular component of the wavevector, $k_{\perp,n}^2=8(n+1)/w_{ch}^2$, precluding pure forward scattering. In Ref. [12] it is shown that the mixed derivative term, $\partial_{\xi z}^2a\sim(\partial_z\phi_\pm)(\partial_\xi\phi_\pm)$, is necessary only when $k_\perp\to0$; thus we can neglect terms proportional to the square of the phase.

Equations (27), (29a), and (29b) form a closed set of equations for predicting the evolution of the Raman forward instability in the presence of an arbitrary pump pulse with both radial and axial variation in the background plasma density. In general the complex phase is a function of ξ, precluding an exact expression for integrals in Eqs. (28a) and (28b). However, we have already ruled out any ξ dependence of the real component of the phase by dropping $\delta\kappa_\pm$. The ξ dependence in the imaginary component of the phase is weak, which allows us to approximate $\phi_\pm(\xi',z)\simeq[1+(\xi'-\xi)\partial_\xi]\phi_\pm(\xi,z)$. With this approximation, the integrals in Eqs. (30a) and (30b) are simply Fourier transforms of the pump pulse vector potential.

Here we will consider the situation where the instability grows over several periods of the plasma modulation: $k_m>\mathrm{Im}[\partial_z\phi_\pm]$. This implies an ordering in our phase evolution model of $k_0^2\gg k_{p,0}^2\sim w_{ch}^{-2}\sim k_0k_m>\mathrm{Im}[\partial_z\phi_\pm]$. Using this disparity of scales, we can average the phase equations over a modulation period. In particular, we use the following:

$$\left\langle\frac{\chi_e}{1+\chi_e}\right\rangle=1-\frac{k^2S(k^2-k_{p,r}^2)}{\sqrt{(k^2-k_{p,r}^2)^2-(\delta k_{p,0}^2)^2}}, \tag{30}$$

where the angled brackets denote the average and the function S represents the sign of the argument and is introduced to ensure that as $\delta\to0$, we retrieve the proper limiting function. Using Eqs. (29a), (29b), (27), and (30) we arrive at the equations describing the evolution of the phase for the Raman forward scattering instability:

$$\frac{\partial\hat{\phi}_+}{\partial z}=\frac{\alpha_0\hat{k}_e}{4\pi A}\left(\frac{\hat{k}_e}{\hat{k}_+}\right)\iint P(r)\left\langle\frac{\chi_e}{1+\chi_e}\right\rangle\left[\bar{\alpha}_0(K_+)e^{-iK_+\xi}+\left(\frac{\alpha_-^*}{\alpha_+}\right)\bar{\alpha}_0(K_-)e^{i(\Phi^*-K_-\xi)}\right]dkd^2r \tag{31a}$$

and

$$\frac{\partial\hat{\phi}_-^*}{\partial z}=\frac{\alpha_0\hat{k}_e}{4\pi A}\left(\frac{\hat{k}_e}{\hat{k}_-}\right)\iint P(r)\left\langle\frac{\chi_e}{1+\chi_e}\right\rangle\left[\bar{\alpha}_0(K_-)e^{-iK_-\xi}+\left(\frac{\alpha_+}{\alpha_-^*}\right)\bar{\alpha}_0(K_+)e^{-i(\Phi+K_+\xi)}\right]dkd^2r, \tag{31b}$$

where $\hat{\phi}_\pm=\phi_\pm+\int\kappa_\pm dz$, $P(r)=|(\hat{z}+\hat{r}\hat{k}_e^{-1}\partial_r)(\vec{u}_0\cdot\vec{u}^*)|^2$, $K_+=k+\hat{k}_e-\partial_\xi\hat{\phi}_+$, $K_-=k+\hat{k}_e+\partial_\xi\hat{\phi}_-^*$, and $\Phi=2\phi_0-\phi_+^*-\phi_-$. The second term occurring in Eqs. (31a) and (31b) arises from the two contributions of the ponderomotive force to the density perturbation, Eqs. (28a) and (28b). If the pump eigenmode differs from the scattered eigenmodes, the second term in the integral will oscillate due to the mismatch in Φ and will not contribute to the instability. In a uniform plasma this would correspond to the waves not being phase matched due to different transverse wavenumbers. In this situation, Eqs. (31a) and (31b) predict that only the redshifted sideband is unstable. On the other hand, if the pump eigenmode matches the sideband eigenmodes (the effective transverse wavenumbers are equal), $\Phi\simeq0$, the sidebands are coupled, and both terms in the integral are important. When $\Phi\simeq0$ both sidebands grow at the same rate. In a transverse uniform plasma this would correspond to the pure forward scattering regime. As we will see in the simulations, the fastest growing mode, in the axially uniform channel, has an eigennumber of $n=1$ with $\Phi\neq0$, but the channel extends to the radial simulation boundary. In a leaky channel [44], a scattered eigennumber of $n=0$ may be the fastest growing mode; thus we choose to examine both situations. We will denote the $\Phi=0$ case as coupled sidebands (each wave has the same transverse eigennumber), and the $\Phi\neq0$ case as uncoupled sidebands. The governing equations for coupled and uncoupled sidebands are

$$\frac{\partial\hat{\phi}_-^*}{\partial z}=\frac{\alpha_0\hat{k}_e^2}{4\pi A}\iint P(r)\left\langle\frac{\chi_e}{1+\chi_e}\right\rangle\left[\hat{k}_-^{-1}\bar{\alpha}_0(K_-)e^{-iK_-\xi}+\hat{k}_+^{-1}\bar{\alpha}_0(K_+)e^{-iK_+\xi}\right]dkd^2r \tag{32a}$$

and

$$\frac{\partial\hat{\phi}_-^*}{\partial z}=\frac{\alpha_0\hat{k}_e}{4\pi A}\left(\frac{\hat{k}_e}{\hat{k}_-}\right)\iint P(r)\left\langle\frac{\chi_e}{1+\chi_e}\right\rangle\bar{\alpha}_0(K_-)e^{-iK_-\xi}dkd^2r, \tag{32b}$$

respectively, where we have defined $\hat{\phi}_\pm=\phi_\pm+\int\kappa dz$.

V. NONLINEAR EVOLUTION FOR WEAK TRANSVERSE VARIATION

Here we derive some simple results where there is no reduction in the exponentiation due to transverse phase mixing. As demonstrated in the next section, the simulation results are consistent with the instability regime described here. In Appendix B, we present the growth rates in the presence of strong transverse phase mixing. In order to obtain solutions in this regime, Eqs. (31a) and (31b) can be simplified to give results resembling spatiotemporal solutions [12,41]. We will skip the algebra in reducing Eqs. (31a) and (31b) and show only the resulting equations describing the evolution of the phase. In the limit of weak transverse variation, we can simply remove any term involving k_p from the transverse integral: $k_{p,r}^2 k_{p,0}^2$.

A. Finite pulse, no modulations

For our simulations, which we describe in the next section, we use the following expression for $\alpha_0(\xi)$:

$$\alpha_0(\xi) = \begin{cases} \hat{\alpha}_0 \sin(\pi\xi/\sigma) & 0 < \xi < \sigma \\ 0 & \text{else} \end{cases}, \tag{33}$$

which has the Fourier transform

$$\bar{\alpha}_0(\zeta) = \frac{\hat{\alpha}_0 \sigma}{\pi}[1 + e^{i\sigma\zeta}]\left[1 - \left(\frac{\sigma\zeta}{\pi}\right)^2\right]^{-1}. \tag{34}$$

From Eqs. (32a), (32b), and (33) we find the phase evolution equations for the coupled and uncoupled sideband situations to be

$$\left(\frac{\partial \breve{\phi}_-^*}{\partial \xi}\right)\left(\frac{\partial \breve{\phi}_-}{\partial z}\right) = -\frac{1}{4}\hat{\alpha}_0^2 I^{pw} \hat{k}_e^2 \left(\frac{k_p}{\hat{k}_-}\right)^2 \sin(\pi\xi/\sigma), \tag{35a}$$

$$\left(\frac{\partial \breve{\phi}^*}{\partial \xi}\right)\left(\frac{\partial \breve{\phi}_-}{\partial z}\right) = -\frac{1}{8}\hat{\alpha}_0^2 I^{pw} \hat{k}_e^2 \left(\frac{k_p}{\hat{k}_-}\right) \sin(\pi\xi/\sigma), \tag{35b}$$

where $\breve{\phi}_- = \hat{\phi}_- \pm \pi\xi/\sigma$ and $I^{pw} \simeq A^{-1}\int P(r) d^2 r$. The maximum growth rate occurs when $\hat{k}_e = k_p \pm \pi/\sigma$. The $\pm$ in our definition of $\breve{\phi}_{n,-}$ refers not to the anti-Stokes and the Stokes sidebands of the pump pulse's central wavenumber, but to the different components of the Stokes sideband due to the envelope of the pump pulse. Solving Eqs. (35a) and (35b) we find

$$\breve{\phi}_- = -i\sqrt{2}\hat{\alpha}_0 (I^{pw})^{1/2}\left(\frac{k_p}{\hat{k}_-}\right)\left(\frac{\hat{k}_e\sigma}{\pi}\right)^{1/2} \times (\hat{k}_e z)^{1/2} \sin^{1/2}\left(\frac{\pi\xi}{2\sigma}\right), \tag{36a}$$

$$\breve{\phi}_- = -i\hat{\alpha}_0 (I^{pw})^{1/2}\left(\frac{k_p}{\hat{k}_-}\right)^{1/2}\left(\frac{\hat{k}_e\sigma}{\pi}\right)^{1/2} \times (\hat{k}_e z)^{1/2} \sin^{1/2}\left(\frac{\pi\xi}{2\sigma}\right). \tag{36b}$$

In Appendix C, we show that the maximum exponentiation occurs when $z = -g/\partial_z g$, where for our pulse shape $g = \sin(\pi\xi/2\sigma)$. This results in a transcendental equation for the position of maximum exponentiation: $c_{g0}t = z + \frac{2\sigma}{\pi}\tan^{-1}(\pi z/2\sigma)$. However, because there can be no exponentiation in regions devoid of the pump, the finite duration of the pulse implies that the maximum exponentiation occurs at the back of the pump pulse. The maximum exponentiation is then

$$\breve{\phi}_- = -i\sqrt{2}\hat{\alpha}_0 (I^{pw})^{1/2}\left(\frac{k_p}{\hat{k}_-}\right)\left(\frac{\hat{k}_e\sigma}{\pi}\right)^{1/2} (\hat{k}_e z)^{1/2}, \tag{37a}$$

$$\breve{\phi}_- = -i\hat{\alpha}_0 (I^{pw})^{1/2}\left(\frac{k_p}{\hat{k}_-}\right)^{1/2}\left(\frac{\hat{k}_e\sigma}{\pi}\right)^{1/2} (\hat{k}_e z)^{1/2}, \tag{37b}$$

which scales as $z^{1/2}$ exponentiation and *not* the usual z exponentiation.

The exponentiation spectrum for each scattered eigenmodes is determined by the coefficient $(I^{pw})^{1/2}$. The uncoupled growth rate [Eq. (37b)] valid for $n > 0$ decreases as a function of eigennumber. The reduction in growth rate for increasing eigennumber occurs because the different eigenfunctions are maximized at different radii. When the maxima occur at similar radii the ponderomotive coupling is stronger and the growth rate increased. For the $n = 0$ pump mode, the maxima are most closely aligned with the nearest n values, resulting in the decreasing growth rate with increasing n. For a different choice of n for the pump mode, the exponentiation would peak around the pump value and decay for larger and smaller eigennumbers.

We note that we can recover the standard infinite pulse Raman growth rates by substituting $\sin(\pi\xi/2\sigma)$ with $\sqrt{2}/2$ (this choice ensures the correct pulse energy scaling) in Eqs. (35a) and (35b) and setting $I^{pw} = 1$ (the plane wave value). With these substitutions we find $\phi_- = -i\frac{1}{\sqrt{2}}\hat{\alpha}_0(k_p/\hat{k}_-)(k_p z)$ and $\phi_- = -i\frac{1}{2}\hat{\alpha}_0(k_p/\hat{k}_-)^{1/2}(k_p z)$ for the coupled and uncoupled sideband cases, respectively.

B. Infinite pulse, modulations

In the presence of modulations, the coupling between the sidebands provides a nonlinear frequency shift, but does not affect the exponentiation. On resonance, the plasma response in the axially uniform and modulated channels reduce to $\langle \chi_e/(1+\chi_e)\rangle \propto (\pm 1/\partial_\xi \phi_\mp)$ and $\langle \chi_e/(1+\chi_e)\rangle \propto (\pm 1/\partial_\xi \phi_\mp)^{1/2}$, respectively. In the axially uniform channel the coupling to the blueshifted sideband reduces the growth rate by providing an effective damping (the negative sign in the response). For the modulated channel, the blueshifted sideband's response is imaginary, providing the frequency shift. As a result, the exponentiation of all scattered eigenmodes is governed by Eq. (32b).

The phase evolution equation for infinitely long pulses $\alpha_0^2(\xi) = \frac{1}{2}\hat{\alpha}_0^2$ with modulations is given by

$$\left(\frac{\partial}{\partial z}\hat{\phi}_-\right)^2\left(\frac{\partial}{\partial \xi}\hat{\phi}_-^*\right) = \frac{1}{\delta}\left(\frac{\hat{\alpha}_0^2 I^{pw}}{8}\frac{\hat{k}_e^2}{\hat{k}_- k_{p,0}}\right)^2 k_{p,0}^2 \hat{k}_e, \tag{38}$$

where I^{pw} is defined in the previous section. The resonant values of $\hat{k}_e$ are $\hat{k}_e^2 = (1 \pm \delta)k_p^2$, corresponding to the plasma density at the maximum and minimum of the modulations. Even though both values of $\hat{k}_e$ are resonant, for $\delta \sim 1$, the

maximum density resonance provides a much larger growth rate. Upon solving for $\hat{\phi}_-$, we find

$$\hat{\phi}_- = -i\frac{3}{4}\delta^{-1/3}(1+\delta)^{-2/3}(I^{\rm pw})^{2/3}\hat{\alpha}_0^{4/3}\left(\frac{\hat{k}_e^2}{2\hat{k}_- k_{p,0}}\right)^{2/3} \times (\hat{k}_e z)^{2/3}(\hat{k}_e\xi)^{1/3}, \tag{39}$$

and upon finding the maximum exponentiation as detailed in Appendix C, we have

$$\hat{\phi}_- = -i\frac{3}{4}\delta^{-1/3}(1+\delta)^{-2/3}(I^{\rm pw})^{2/3}\hat{\alpha}_0^{4/3}\left(\frac{\hat{k}_e^2}{2\hat{k}_- k_{p,0}}\right)^{2/3}(\hat{k}_e z). \tag{40}$$

Comparing Eq. (40) with the infinite pulse result in a axially uniform channel $\phi_- = -i\frac{1}{2}\hat{\alpha}_0(I^{\rm pw})^{1/2}(k_p/\hat{k}_-)^{1/2}(k_p z)$, we see that the fractional powers are altered by the presence of modulations, and that larger modulation amplitudes reduce the growth rate. For $\delta \sim 1$ the exponentiation in the modulated channel is smaller through the stronger enhanced scalings with α_0 and $k_p/\hat{k}_-$. Equations (38)–(40) do not directly limit to the growth rates found in the axially uniform situation as one takes the limit as $\delta \to 0$. This is a result of the approximation $\delta k_{p,0} \gg |\partial_\xi \hat{\phi}_\pm|$ used in simplifying Eq. (32b). This is a valid approximation for the modulations considered here as $\delta \sim 1$. If δ is chosen to be too small, one may expect the growth rates in Eqs. (35a) and (35b) to hold instead.

C. Finite pulse, modulations

Direct manipulation of Eq. (32b) to provide an equation describing the evolution of the complex phase for finite pulses in the presence of density modulations is difficult. We can, however, come up with a heuristic scaling based on the results of the previous two sections. From Eqs. (36b) and (37b) we see that the maximum growth rate entails evaluating a function of the pulse shape at $\xi = -\sigma$, the back of the pulse where the exponentiation is maximized. We can get the scaling with respect to z by comparing Eqs. (37b) and (39). Based on these equations our ansatz for the growth is

$$\hat{\phi}_- = -i\delta^{-1/3}(1+\delta)^{-2/3}(I^{\rm pw})^{2/3}\hat{\alpha}_0^{4/3}\left(\frac{\hat{k}_e^2}{\hat{k}_- k_{p,0}}\right)^{2/3}\left(\frac{\hat{k}_e\sigma}{\pi}\right)^{1/3}(\hat{k}_e z)^{2/3}, \tag{41}$$

where the numerical coefficient of unity is based on the results of simulations presented in the next section. Comparing Eqs. (37b) and (41) we see that modulations are most effective at smaller amplitudes and longer pulse lengths. Figure 1 shows a comparison of the exponentiation for the modulated and uniform cases as a function of z for a pump amplitude of $\hat{\alpha}_0 = 0.25$ and the $n = 1$ scattered spatial harmonic. At large propagation distances the growth in the modulated plasma would become larger, but as shown in the simulations in the next section saturation of the instability occurs earlier. For quasiphase-matched direct acceleration, the quantity $\sigma\hat{\alpha}_0$ should be maximized for the largest energy gain. Based on Eq. (41), increasing the pulse length is preferable to increasing the amplitude due to the weaker scaling of Raman growth rate with pulse length.

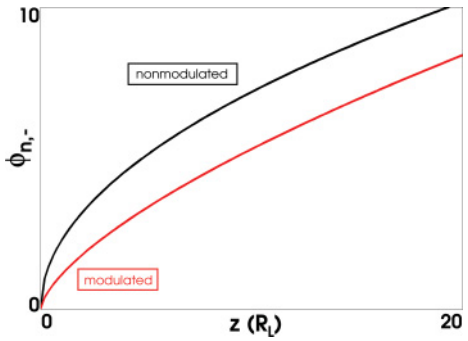

FIG. 1. (Color online) A comparison of the exponentiation in transversely uniform plasmas in the axially uniform case, the black (upper) line, and the modulated case, the red (lower) line), as a function of propagation distance. The pump amplitude is $\hat{\alpha}_0 = 0.25$, and the scattered eigennumber is $n = 1$.

VI. SIMULATIONS

In the previous section, we examined simple analytic results for the exponentiation of the Raman forward instability. The results, however, were limited to analytically tractable situations. We now present the results of WAKE simulations [42], allowing us to see which effects dominate in a more realistic setting where an interplay between effects is possible.

WAKE is a fully relativistic, nonlinear, kinetic simulation tool for modeling the propagation of short laser pulses in underdense plasmas. WAKE is a moving window, particle-in-cell simulation, but utilizes the disparity of two timescales to significantly reduce computational times: the plasma response time compared to the central pulse frequency, and the pulse evolution time compared to the electron transit time through the pulse. For tenuous plasmas ($\omega_p^2 \ll \omega_0^2$), the electron response can be separated into a high-frequency and a ponderomotive component. Upon averaging over the rapid pulse-induced oscillations, the plasma motion needs to be resolved only at the plasma period. In addition, the pulse modification timescale plasma is solely a function of the wave frame coordinate ξ. Because the evolution of the laser envelope is slow compared to the transit time of electrons through the pulse, the field solver for the laser pulse does not need to be updated after every particle time step. Using these simplifications, WAKE solves an envelope equation for the time evolution of the pulse in one transverse and one longitudinal dimension. Inclusion of group velocity dispersion to lowest order in ω_p/ω_0 allows for longitudinal modifications to the pulse. The pulse is self-consistently altered by the ponderomotively driven plasma current through the source in the envelope equation. We note that for the channels and pulses considered here $\omega_p^2/\omega_0^2 \sim 0.004$ and $\sigma/R_T \sim 0.3$,

where $R_T = \pi w_{ch}^2/c\lambda$ is the Rayleigh time. While the first assumption is well justified, the second is marginal but can be relaxed by reducing the laser pulse evolution time step.

We simulate the propagation of a radially polarized laser pulse initialized as the lowest-order radial eigenmode in the density profile given in Eq. (2), which extends to the transverse simulation boundary. The pulse shape has the form of Eq. (33) with a total length of $\sigma = 1$ps. The central wavelength is $\lambda = 800$ nm, the spot size is $w_{ch} = 15\mu$m, and the amplitude $\hat{\alpha}_0$ will be varied. The background plasma density is $n = 7 \times 10^{18}\text{cm}^{-3}$, and we will consider both nonmodulated, $\delta = 0$, and modulated, $\delta = 0.9$, channels with a modulation period $2\pi/k_m = 350\mu$m. The simulation follows the pulse propagation in a 1.6 ps window over $40R_T$ or 3.5cm.. The radial boundary is set at 120 μm or $8w_{ch}$. The simulation grid has 2000 points in ξ with a length of 480 μm and 640 points in r, which well resolves the plasma period in both directions.

To examine the growth of the instability, we extract the vector potential from the simulation and perform a Fourier-Gaussian-Laguerre decomposition as follows:

$$a_n(k_z,t) = \frac{1}{n+1}\int\int e^{ik_z\xi - r^2/w_{ch}^2} L_n^1\left[\frac{2r^2}{w_{ch}^2}\right] a(r,\xi,z) r^2 d\xi dr. \tag{42}$$

As we will see the instability has a linear stage and a saturation stage. To extract the exponentiation to compare with the results of the theory section we define the local growth rate as

$$\phi_n(z) = \frac{1}{2}\log_e\left|\frac{a_n(k_{\text{res}},z)}{a_n(k_{\text{res}},0)}\right|^2, \tag{43}$$

where k_{res} is the wavenumber corresponding to maximum growth.

Figures 2(a) and 2(b) show the maximum exponentiation as a function of z for the $n = 0$ and $n = 1$ scattered radial eigenmodes, respectively, driven with a pump amplitude of $\hat{\alpha}_0 = 0.14$ in an axially uniform channel. The wavy lines are the simulation results smoothed over five points, the smooth

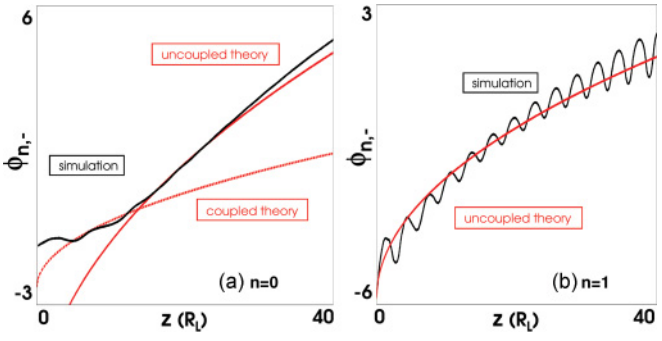

FIG. 2. (Color online) A comparison of our theoretical exponentiations with the simulation results in an axially uniform channel for a pump amplitude of $\hat{\alpha}_0 = 0.14$. (a) $n = 0$ scattered eigenmode; (b) $n = 1$ scattered eigenmode. The black (oscillating) lines are the simulation results, the red (solid) lines are the uncoupled sideband theory results, and the red dashed is line the coupled sideband theory result.

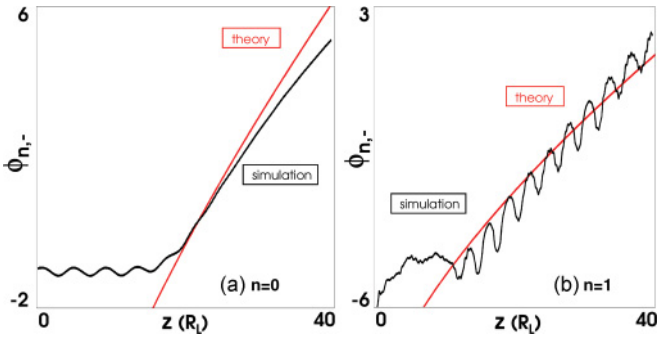

FIG. 3. (Color online) A comparison of our theoretical exponentiations with the simulation results in a modulated channel for a pump amplitude of $\hat{\alpha}_0 = 0.21$. (a) $n = 0$ scattered eigenmode; (b) $n = 1$ scattered eigenmode. The black oscillating lines are the simulation results, and the red lines are the theory results.

line (red online) is the prediction of the uncoupled theory, and the dashed line (red online) the prediction of the coupled theory. The oscillations in Fig. 2(b) are due to the second term in Eq. (31b), which oscillates due to the mismatch in Φ. In Fig. 2(a) the exponentiation starts in the coupled regime, and as the instability grows the sidebands decouple. As the scattered $n = 0$ eigenmode amplitude grows, it acquires a nonlinear phase shift detuning it from the pump, resulting in the transition to the decoupled growth rate. In Fig. 2(b), the sidebands are always uncoupled.

In Figs. 3(a) and 3(b) the maximum exponentation as a function of z for the $n = 0$ and $n = 1$ scattered radial eigenmodes in the modulated channel is plotted. Here the pump amplitude was $\hat{\alpha}_0 = 0.21$. For both the $n = 0$ and $n = 1$ cases the sidebands are always uncoupled as discussed in the previous section. From the agreement with the theory it is apparent that the instability evolves with little damping due to the transverse phase mixing.

In Fig. 4, the exponentiations in the axially uniform and modulated channels are compared for two different amplitudes. The theory results match reasonably well for $\hat{\alpha}_0 = 0.28$ until the instability saturates. As expected the modulated channel has less exponentiation prior to saturation due to the reduced exponentiation. The instability saturates in

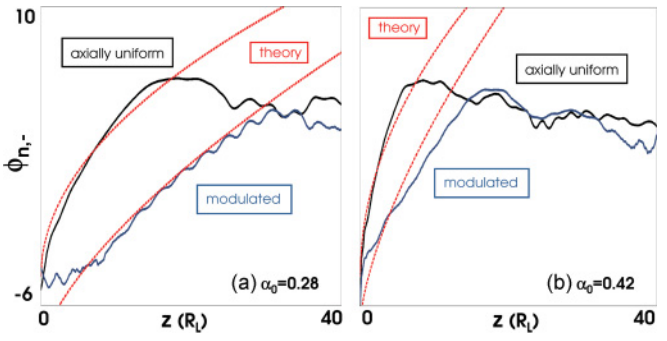

FIG. 4. (Color online) A comparison of the growth in the axially uniform and modulated plasma channels as a function of propagation distance. (a) Initial pump amplitude is $\hat{\alpha}_0 = 0.28$; (b) amplitude is $\hat{\alpha}_0 = 0.42$. The dashed red line is the theory, the black solid (upper) line is the axially uniform exponentiation, and the blue solid (lower) line is the modulated exponentiation.

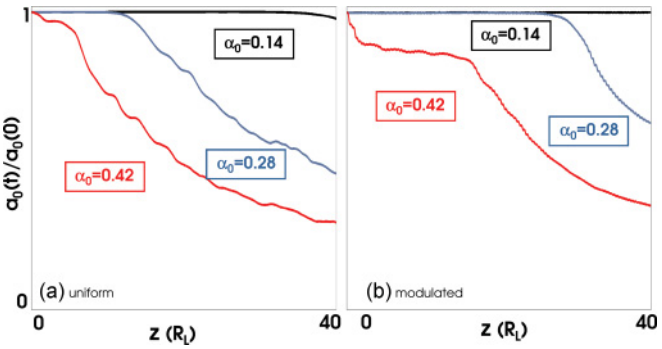

FIG. 5. (Color online) Normalized pump amplitude as a function of time for three different initial amplitudes. (a) Axially uniform channel; (b) modulated channel. The black (topmost) line is for a pump amplitude $\hat{\alpha}_0 = 0.14$, the blue (middle) line is for $\hat{\alpha}_0 = 0.28$, and the red (lowest) line is for $\hat{\alpha}_0 = 0.42$.

two ways: pump depletion and rescattering of the scattered sideband. Pump depletion occurs due to the finite energy available at wavenumbers within the initial bandwidth of the central wavenumber. The instability transfers pulse energy from the central wavenumber to the scattered wavenumber reducing the amplitude and as a result the growth rate. Once the initial sideband has reached high enough amplitude (by gaining energy from the pump pulse), it rescatters producing its own sidebands to which its energy is transferred. Each additional sideband can undergo the rescattering producing energy diffusion in the spectral domain, which we refer to as cascading. The larger the field amplitude the earlier the onset of both pump depletion and rescattering. This is observed by the earlier saturation for the instability in Fig. 4(b). Pump depletion and rescattering will be examined further below.

Figures 5(a) and 5(b) demonstrate the relative importance of pump depletion in the amplitude scaling of Fig. 3. In Fig. 5(a) and 5(b) the normalized pump amplitude

$$\bar{a}_0 = \left[\frac{\int |\vec{a}_0(k,z)|^2 \, dk}{\int |\vec{a}_0(k,0)|^2 \, dk} \right]^{1/2}, \tag{44}$$

where we have integrated from $k = k_0 - \frac{1}{2}k_{p,0}$ to $k = k_0 + \frac{1}{2}k_{p,0}$, as function of time for the axially uniform and modulated situations, respectively, is plotted for three different initial amplitudes $\hat{\alpha}_0 = 0.14$, $\hat{\alpha}_0 = 0.28$, and $\hat{\alpha}_0 = 0.42$. For larger amplitude the pump is depleted faster and the instability growth rate is increasingly reduced, due to a reduction in the effective pump amplitude. As expected the increased growth rate in the axially uniform case results in a more rapid decay in the pump amplitude than in the modulated situation. In particular, pump depletion becomes appreciable when $\phi_n(z) \sim \ln(\hat{\alpha}_0/\hat{\alpha}_n)$; thus because ϕ_n is smaller in the modulated case, the onset of depletion also occurs later for $\hat{\alpha}_0 = 0.28$.

For $\hat{\alpha}_0 = 0.42$ the pump initially depletes faster in the modulated channel, explaining the early saturation of the exponentiation and deviation from the theory in Fig. 4(b). This is in part due to the nonlinear effect of self-focusing. The pulse in the modulated channel experiences an effective density of $n_e \sim (1+\delta)n_0$ every half period. In these regions the critical power for self-focusing and pulse compression,

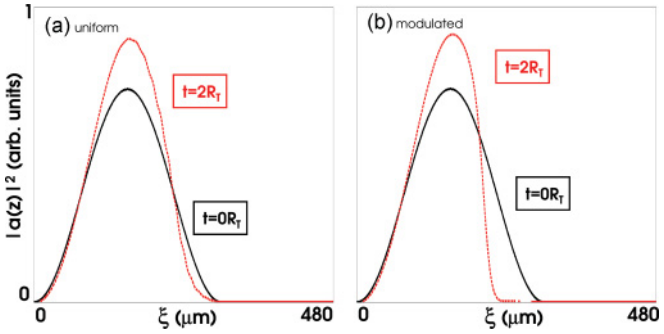

FIG. 6. (Color online) Longitudinal pulse shape at two different times during the propagation. (a) Uniform channel; (b) modulated channel. The black solid line is the pulse shape at $0R_T$, and the dashed red line is at $2R_T$.

$P_{cr} = 17(\omega^2/\omega_p^2)GW$, drops by a factor of ~2, making our value of $P/P_{cr} \sim 1/3$, while in the alternative regions of low-density $P/P_{cr} \sim 1/60$ [45]. In this regime the modification to the background density becomes significant, and the propagating modes are no longer eigenmodes of the original density profile [Eq. (2)]. The pump depletion results from a competition between a reshaping of the $n = 0$ eigenmode and forward Raman scattering. Figures 6(a) and 6(b) show the pulse shape of the axially uniform and modulated channels, respectively, at the maximum of the pulse amplitude, $r = w_{ch}/\sqrt{2}$, for $z = 0$ and $z = 2R_T$. The smaller value of P_{cr} in the half regions of modulation periods result in stronger pulse steepening. This effect will be explored further in a forthcoming publication.

Figures 7(a) and 7(b) depict $\log_e[a_n(k_z,z)]$ for the central and first redshifted sideband of the nonmodulated and modulated cases, respectively. The eigenmode plotted is $n = 1$ and the initial amplitude $\hat{\alpha}_0 = 0.28$. The maximum growth rates for the initial redshifted side band are at $k = k_0 - k_{p,0}$ and $k = k_0 - (1+\delta)^{1/2}k_{p,0}$ for the nonmodulated and modulated cases, respectively, the same values as predicted by our theory. The $k = 0$ spectrum is at lower amplitude because the pulse is initialized as the $n = 0$. The long-period oscillation visible in both plots is due to the $n = 1$ mode having a group

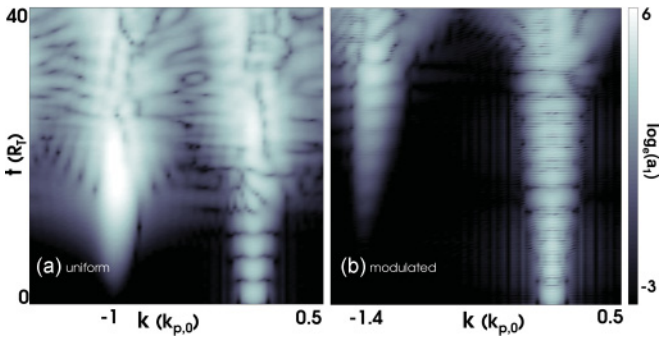

FIG. 7. (Color online) Log scale of the electromagnetic spectrum as a function of time for the $n = 1$ eigenmode. Figure (a) is the axially uniform channel and (b) the modulated channel. The right streak in each curve is the seed level of the eigenmode at the pump central wavenumber. The left streak is the first Stokes sideband resulting from the scattering instability.

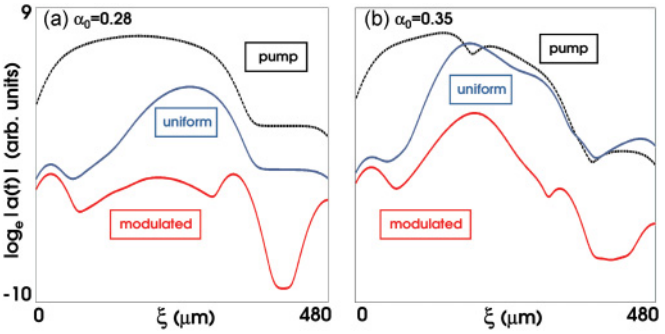

FIG. 8. (Color online) Laser pulse shape for the pump wave, black dashed line (top), and scattered waves of the $n = 1$ spatial harmonic in the axially uniform, blue solid line (middle), and modulated, red solid line (lower), channels evaluated at the k_z for maximum growth on a log scale as a function of ξ. (a) Pump amplitude $\hat{\alpha}_0 = 0.28$; (b) pump amplitude $\hat{\alpha}_0 = 0.35$.

velocity different than c, the speed of the moving window. The modulation period is visible as the rapid oscillation in the modulated plot. The figure shows that the nonmodulated instability reaches saturation at $\sim 15 R_T$ while the modulated case saturates closer to $\sim 35 R_T$, a result of the reduced modulated growth rate.

In the previous section, we found an ansatz analytic result for how the pump pulse variation affects the growth of the Raman forward instability in transversely uniform plasmas but were stuck with a complex differential functional in the channeled case that provided little insight. To examine the growth of the instability in the pulse frame we perform a windowed Fourier transform of the vector potential as follows:

$$a_n(k_z,\xi',z) = \frac{1}{n+1}\int\int e^{ik_z\xi - r^2/w_{ch}^2 - (\xi-\xi')^2/W^2} \times L_n^1\left[\frac{2r^2}{w_{ch}^2}\right] a(r,\xi,z) r^2 d\xi dr, \quad (45)$$

where we have found that the width $W \sim 24\mu$m (80 fs) provides adequate resolution in ξ. We note Eq. (45) is Eq. (42) with an additional Gaussian factor for the window. That is, Eq. (42) provides a better indication of the maximum growth rate for each radial eigenmode, while Eq. (45) provides the localized perturbation. Figure 8 shows $\log_e |a_n(k_z,\xi',z)|$ for the $n = 1$ radial eigenmode at $z/c = 10 R_T$ evaluated at the k_z corresponding to maximum growth as a function of pulse coordinate. In Fig. 8(a) the pump amplitude is $\hat{\alpha}_0 = 0.28$, while in Fig. 8(b) $\hat{\alpha}_0 = 0.35$. In both cases the growth of the scattered wave's pulse shape does not mimic the exact pulse shape of the laser, but is localized to within the pump pulse's envelope. The scattered wave's envelope grows until reaching the back of the pump pulse where the pump amplitude goes to zero. By $z/c = 10 R_T$ for the $\hat{\alpha}_0 = 0.35$ pump, the scattered wave in the axially uniform channel has already reached the pump amplitude.

Having demonstrated that transverse phase mixing plays little role in the linear stage of the instability, and that modulations reduce the exponentiation of the instability, we now consider the nonlinear stage where cascading plays a role. As a qualitative consideration, we plot the pulse shape after $30 R_T$ of propagation in both the modulated and nonmodulated channels in Fig. 9 for $\hat{\alpha}_0 = 0.35$. The top plots are modulated channels and the bottom the axially uniform. The plasma density has been plotted in the background for reference. After $30 R_T$, the pulse in the modulated channel has dropped in amplitude but has maintained its shape, while the pulse in the axially uniform channel has become both modulated, at the fundamental plasma period, and transversely diffuse, an indication of strong scattering to higher-order eigenmodes.

Figures 10(a) and 10(b) show the spectrum for the $n = 0$ eigenmode in the axially uniform and modulated channels, respectively, as a function of propagation time for a pump amplitude of $\hat{\alpha}_0 = 0.28$. The pump pulse spectrum is visible as the feathering away from the central peak. Previously we only

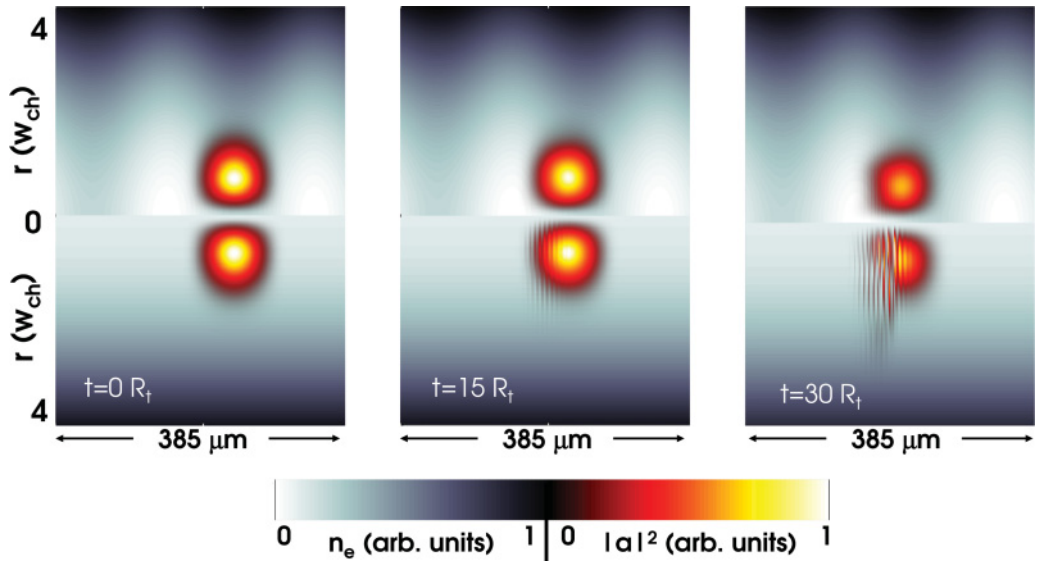

FIG. 9. (Color online) Laser pulse shape at three different times in a modulated channel (top) and an axially uniform channel bottom for an initial amplitude of $\hat{\alpha}_0 = 0.35$.

considered the initial redshifted sideband at $k = k_0 - k_{p,0}$. Because of the larger growth rates in the axially uniform channel, the initial sideband peaks appear brighter than for the modulated channel. It is clear from Fig. 10 that rescattering has occurred and field energy has cascaded to both lower and higher wavenumbers. This effect has been studied in detail in uniform plasmas by Mima and Nahikawa [3]. Here we consider the results in axially uniform and modulated channels qualitatively and leave a detailed analysis for a future publication.

As the amplitude of the initial redshifted sideband increases, it also undergoes Raman forward scattering, producing its own sideband at $k = k_0 - 2k_{p,0}$, the second sideband creates a third, and so on. Figure 10 shows that in spite of being stable, the blueshifted sidebands, $k = k_0 + mk_{p,0}$, grow in amplitude, but the growth lags behind the corresponding redshifted band, $k = k_0 - mk_{p,0}$. To explain the growth of the blue sidebands we consider the coupled Eq. (31b). When calculating the growth rates for the "uncoupled" regime we simply dropped the second term in Eq. (31b), which couples the blue sideband to the red sideband. However, as the red sideband grows in amplitude, this sideband coupling becomes significant and overcomes the noncoupled term. The result is that the red sideband "pulls up" the amplitude of the blue sideband. Rescattering takes longer to initiate in the modulated channel due to the reduced growth rate: it takes longer for each additional sideband to reach the required amplitude such that its own scattering is appreciable. The onset of growth for each additional sideband occurs before its pump (the sideband appearing earlier in time at smaller k) has reached a steady state due to saturation. Thus, each successive scatter cannot be considered as an independent instability with a steady-state pump.

In the previous section, we found that the exponentiation in the modulated channel was maximized when $\hat{k}_e^2 = (1+\delta)k_{p,0}^2$, corresponding to a resonance with the maximum plasma density. For a density profile, where the laser pulse spends less time in the vicinity of the maximum density, we would expect less growth. In particular we consider the periodic triangular density profile

$$\omega_p^2(r,z) = \begin{cases} \omega_{p,0}^2\left[1+\delta\left(\frac{k_m z}{\pi}\right)\right] + \frac{1}{2}\omega''^2_{p,0} r^2 & 0 \leqslant \mathrm{mod}(k_m z, 2\pi) < \pi \\ \omega_{p,0}^2\left[1+2\delta-\delta\left(\frac{k_m z}{\pi}\right)\right] + \frac{1}{2}\omega''^2_{p,0} r^2 & \pi \leqslant \mathrm{mod}(k_m z, 2\pi) < 2\pi \end{cases}. \tag{46}$$

Note that this function decays away from the maximum much more rapidly than Eq. (2): The derivative in the vicinity of the maximum is finite for Eq. (46) and zero for Eq. (2). Figure 11 shows a comparison of simulation results of the $n = 1$ scattered eigenmode using the density profiles in Eqs. (2) and (46) for a pump amplitude of $\hat{\alpha}_0 = 0.35$. Figure 11(a) shows the maximum exponentiation of the scattered for the first redshifted sideband. As expected the growth is reduced in the triangular profile compared to the sinusoidal profile. Figures 11(b) and 11(c) show the resulting spectra.

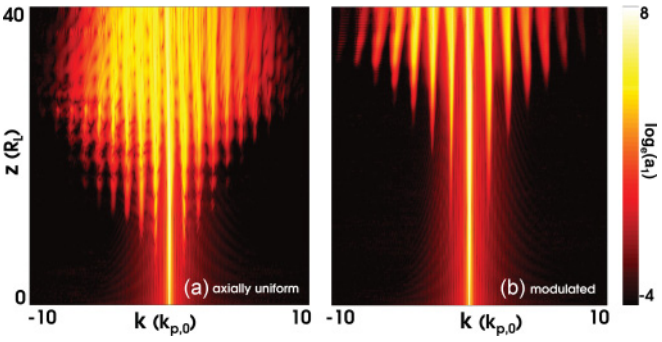

FIG. 10. (Color online) Log scale of the electromagnetic spectrum as a function of time for the $n = 0$ eigenmode and a pump amplitude of $\hat{\alpha}_0 = 0.28$. (a) Channel is axially uniform; (b) channel is modulated.

VII. SUMMARY AND CONCLUSIONS

We have developed an analytic model for the exponentiation of the Raman forward instability in modulated plasma channels. The model describes the complex phase evolution of eigenmodes within the channel generated from the scattering of a pump laser eigenmode scattering off fluctuations in the plasma density. After deriving the governing equation, we focused on the parameter regime of many plasma oscillations per pulse length. We also limited our analysis to radial polarized modes, but the analysis for linearly polarized modes

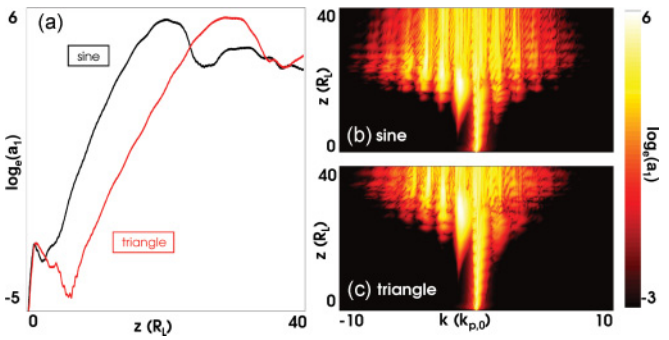

FIG. 11. (Color online) A comparison of an axial sinusoidal and triangular density profile for the $n = 1$ eigenmode and a pump amplitude of $\hat{\alpha}_0 = 0.35$. (a) Maximum exponentiation is plotted for the initial redshifted sideband as a function of propagation distance. The black line (left) and the red line (right) correspond to the sine and triangle profiles, respectively. (b) and (c) Spectra of the scattered eigenmode as a function of time in the sinusoidal and triangular channels.

is different only by constants in the diffractive contribution to the dispersion and changes in the ponderomotive overlap integrals; the phenomenology is the same. With the model we examined two regimes of the instability: a weak transverse variation regime and a transverse phase-mixing-dominated regime. In both axial uniform and modulated channels, for parameters of interest, we find that phase mixing due to the transverse variation of the channel does not play a role in the instability growth.

For the situation with weak transverse variation, we analytically considered the evolution of the phase for finite pulse lengths. In these situations, the modulations resulted in a modified scaling of the growth rate. In particular the growth rate was found to scale as $\sim(k_{p,0}/k_0)^{2/3}\alpha_0^{4/3}$ as opposed to the standard $\sim(k_{p,0}/k_0)^{1/2}\alpha_0$. The finite duration of the pulse was found to have a significant affect on the exponentiation. For long pulses, the position of maximum growth occurs at $z = c_g t/2$; however, for short pulses, this position moves outside the pulse early in the propagation. Thus the maximum growth in the short pulse occurs at the back of the pulse, resulting in an exponentiation that scales as $\sim z^{1/2}$ not $\sim z$.

In the strong transverse phase-mixing regime, the plasma resonance in axially uniform channels results from an essential singularity in the coupling, a single radius allowing for local phase matching. The plasma resonance in the modulated channel contains no essential singularity. In the modulated case, the resonance is spread over a range of radii determined by the amplitude of the modulations. This is the result of global phase matching taking place at a point in r-z space that oscillates in the lab frame. The transverse spreading of the resonance results in Raman forward growth rates that are 2–3 times smaller than those in axially uniform channels.

The analytically predicted weak transverse growth rates were verified using WAKE simulations. Comparisons of the simulations and theory for small pump amplitudes demonstrated exponentiation scalings with pump amplitude and scattered eigennumber. For larger pump amplitudes, the pump eigenmode is rapidly depleted, and the linear eigenmodes become distorted as the incident power begins to approach the critical power for self-focusing. In spite of the reduced exponentiation in the modulated channels, at large amplitudes, the pump initially depleted faster than in the axially uniform channel. The modulated channels have regions of higher density than in uniform channels, resulting in an oscillation of the critical power and stronger pulse compression. Finally the simulations predicted that each Raman forward sideband is forward scattered itself, resulting in a cascade. As the amplitude of each sideband grows, so too does its rate of transfer of energy to its own sidebands. The transfer of energy between sidebands saturates the instability and causes a diffusion of energy in spectral space. The cascade was found to be asymmetric for the Stokes and anti-Stokes bands. The Stokes sidebands start stable but eventually become unstable due to being "dragged" up by the anti-Stokes sidebands. The wavenumbers of maximum growth matched those predicted by our model.

The main result of the analysis and simulations is to demonstrate that modulated channels allow the guiding of pulses with larger amplitudes or longer propagation distance than axially uniform channels. For quasiphase-matched direct acceleration, this allows the pulse shape to be maintained for further distances extending the acceleration length. In modern laser wakefield experiments, the laser duration is typically shorter than a plasma period; thus Raman scattering does not play a role. However, density modulations would affect the structure of the wakefield. For instance, one would expect higher fields and less dephasing of the electrons with the wakefield in the low-density regions, while the opposite is the case in the high-density regions. Examining the role of density modulations in wakefield acceleration will be considered in a later publication.

ACKNOWLEDGMENTS

The authors would like to acknowledge support from NSF, DOE, and ONR. We would also like to thank H. M. Milchberg, C. Schroeder, S. Kalmykov, and C. Joshi for fruitful discussions.

APPENDIX A: WAVE ACTION

Here we show that the conserved wave action can be expressed as a sum over the imaginary components of the phase. The wave action can be expressed as

$$\mathrm{A} = \int d\xi d^2 r \left[\vec{a} \cdot \frac{\partial \vec{a}^*}{\partial z} - \vec{a}^* \cdot \frac{\partial \vec{a}}{\partial z} \right], \tag{A1}$$

where using Eqs. (9), (11), (28), and (29), we have for our system

$$\vec{a}(\vec{x},t) = \alpha_0(\xi)\vec{u}_0(\vec{x}_\perp) e^{i(\hat{k}_0 z - \omega_0 t) + i\phi_0(\xi,z)} + \sum_{\pm,n} \alpha_{n,\pm}\, \vec{u}_{n,\pm}(\vec{x}_\perp) e^{i(\hat{k}_\pm z - \omega_\pm t) + i\phi_{n,\pm}(\xi,z)}. \tag{A2}$$

Upon averaging over the rapid timescale, and integrating we have simply

$$\langle \mathrm{A} \rangle = \int d\xi \sum_j |\beta_j(\xi)|^2 e^{-2\mathrm{Im}[\phi_j(\xi,z)]} \left\{ k_j + \frac{\partial}{\partial z} \mathrm{Re}[\phi_j(\xi,z)] \right\}, \tag{A3}$$

where the angled brackets represent the averaging, the index j sums all over all n, anti-Stokes and Stokes modes, the pump, and β_j are the coefficients resulting from projecting each mode onto itself and integrating over radius. For an infinite pulse, we write the differential action

$$\frac{d\langle \mathrm{A} \rangle}{d\xi} = \sum_j |\hat{\alpha}_j|^2 e^{-2\mathrm{Im}[\phi_j(z)]} \left\{ k_j + \frac{\partial}{\partial z} \mathrm{Re}[\phi_j(z)] \right\}, \tag{A4}$$

where we have used the fact that the radial eigenmodes all have the same integrated area to write the action coefficients in terms of the seed amplitudes only. Thus the total differential action is directly proportion to a sum over the real component of the phase for all waves in the system, and the imaginary component describes the transfer of action between waves. The growth rates can evolve only to maintain the constancy of the action.

APPENDIX B: NONLINEAR EVOLUTION WITH TRANSVERSE PHASE MIXING

Transverse phase mixing played little role in the exponentiation for the simulation parameters considered. This may not be the case, however, for longer pulses or deeper channels. Weak transverse variation $\partial_\xi \hat{\phi}^*_{n,-}$ cannot be neglected regardless of the pulse length. Here we consider a situation where $k_{p,0}\partial_\xi \hat{\phi}^*_{n,-} \ll w_{ch}^{-2}$ such that $\partial_\xi \hat{\phi}^*_{n,-}$ can be neglected. In this situation, the instability behaves in the strongly damped regime, where the damping is provided by the transverse phase mixing. For simplicity we will also use the condition $w_{ch}^{-2} \ll k_{p,0}^2$ such that only the longitudinal component of the ponderomotive force need be considered. This will provide insight into the difference between the exponentiation reduction due to the transverse and longitudinal uniformities. The primary difference in the strong transverse phase-mixing case is that the plasma resonance must be integrated over radius.

1. Infinite pulse, no modulations

To consider the limit of infinite pump pulse length, we set $\alpha_0^2(\xi) = \hat{\alpha}_0^2/2$ for all ξ. The choice of $\alpha_0^2(\xi) = \alpha_0^2/2$ provides the same energy scaling with pulse length and amplitude as the pulse used in the simulations [Eq. (33)]. After performing some algebra, we find the phase evolution for the coupled and uncoupled sidebands to be

$$\frac{\partial}{\partial z}\hat{\phi}_{n,\pm} = -i\frac{\pi}{2}\hat{\alpha}_0^2\left(\frac{\hat{k}_e}{\hat{k}_\pm}\right)(\hat{k}_e w_{ch})^2 P(r_*)\hat{k}_e, \tag{B1a}$$

$$\frac{\partial}{\partial z}\hat{\phi}_{n,\pm} = -i\frac{\pi}{4}\hat{\alpha}_0^2\left(\frac{\hat{k}_e}{\hat{k}_\pm}\right)(\hat{k}_e w_{ch})^2 P(r_*)\hat{k}_e, \tag{B1b}$$

where

$$r_*(k_e) = \tfrac{1}{2}w_{ch}^2\left[\hat{k}_e^2 - k_{p,0}^2\right]^{1/2}, \tag{B2}$$

and $\hat{k}_e^2 = k_p^2(r_*)$. We note that both sidebands are unstable, the $(\hat{k}_e/\hat{k}_-)$ scaling of Eqs. (B1a) and (B1b) are the same, and the equations are different only by a factor of 2. This is in contrast to the weak transverse variation case, where the dependence on $\partial_\xi \hat{\phi}^*_{n,-}$ broke the symmetry between the two sidebands, resulting in the weaker scaling with $(\hat{k}_e/\hat{k}_-)$ when the sidebands were coupled. The transverse variation has resulted in phase mixing. From the scaling with $\hat{\alpha}_0^2$ we see that the phase mixing results in the plasma wave evolving in a strongly damped regime. To find the wavevector associated with the plasma wave we look for $\hat{k}_e$ that maximizes the right-hand side of Eqs. (B1a) and (B1b). In Appendix D, we examine why the growth rate increases with increasing w_{ch}. Because of the similarity of results, we will focus on the Stokes sideband and the coupled sideband situation henceforth.

2. Infinite pulse, modulations

Upon integrating over k and using the delta function from $\bar{\alpha}$, we find the phase evolution for the Stokes sideband in the presence of modulations to be

$$\frac{\partial}{\partial z}\hat{\phi}_- = -\frac{4}{\pi}i\hat{\alpha}_0^2\left(\frac{\hat{k}_e}{\hat{k}_-}\right)\hat{k}_e\frac{k_{p,0}^2}{w_{ch}^2} \times \int \frac{P(r)}{\sqrt{\left(\delta k_{p,0}^2\right)^2 - \left(\hat{k}_e^2 - k_{p,r}^2\right)^2}}d^2r, \tag{B3}$$

where we have dropped the minus one in Eq. (30) as it will contribute only a phase. From Eq. (B3), we see that the only contributions to the growth rate will come from radii within the channel that satisfy the condition

$$\frac{1}{4}w_{ch}^2\left[\hat{k}_e^2 - k_{p,0}^2(1+\delta)\right] < \left(\frac{r}{w_{ch}}\right)^2 < \frac{1}{4}w_{ch}^2\left[\hat{k}_e^2 - k_{p,0}^2(1-\delta)\right], \tag{B4}$$

where the sign of δ has been taken as positive. Thus, as opposed to Eq. (B1a), instead of one radius contributing to the resonance, a range of radii of width $\Delta r^2/w_{ch}^2 = \frac{\delta}{2}(k_{p,0}w_{ch})^2$ contribute to the resonance. It is worth noting that this range of radii can be quite large as $(k_{p,0}w_{ch})^2 \gg 1$, and the resonance can be spread over a large transverse region of the channel. Furthermore Eq. (B4) shows that $\hat{k}_e^2 > (1+\delta)k_{p,0}^2$ to ensure that the range of resonant radii is strictly real.

One can show that for small delta, approximating $P(r) \simeq P(r_*)$, and integrating over the interval in Eq. (B4) reproduces Eq. (B1a). For further comparison we consider scattering in the coupled situation where the scattered eigenmode has $n = 1$. In the nonmodulated and modulated cases, respectively, we have the following:

$$(\partial_z\hat{\phi}_-)_{\delta=0} = -i\frac{\pi}{32}\hat{\alpha}_0^2\left(\frac{\hat{k}_e}{\hat{k}_-}\right)\hat{k}_e(\hat{k}_{p,0}w_{ch})^2 \times \left(\hat{k}_e^2 - k_{p,0}^2\right)^2 w_{ch}^4 e^{-(\hat{k}_e^2 - k_{p,0}^2)w_{ch}^2}, \tag{B5}$$

$$\frac{(\partial_z\hat{\phi}_-)_{\delta\geqslant 0}}{(\partial_z\hat{\phi}_-)_{\delta=0}} = \left[1 + \left(\frac{\delta k_{p,0}^2}{\hat{k}_e^2 - k_{p,0}^2}\right)^2\right]I_0 - \left(\frac{\delta k_{p,0}^2}{\hat{k}_e^2 - k_{p,0}^2}\right)\left[2 + \frac{1}{w_{ch}^2}\left(\frac{1}{\hat{k}_e^2 - k_{p,0}^2}\right)\right]I_1, \tag{B6}$$

where I_a are the modified Bessel functions evaluated at $\delta k_{p,0}^2 w_{ch}^2$. The first and second equations are maximized at approximately $(\hat{k}_e w_{ch})^2 \simeq 2 + (k_{p,0}w_{ch})^2[1 + \delta I_1/I_0]$ where $\delta = 0$ in the prior case. Figure 12(a) shows a comparison of Eqs. (B5) and (B6) as a function of $(\hat{k}_e w_{ch})^2$ for a plasma density $7 \times 10^{18}\,\mathrm{cm}^{-3}$, matched spot size of 15μm,

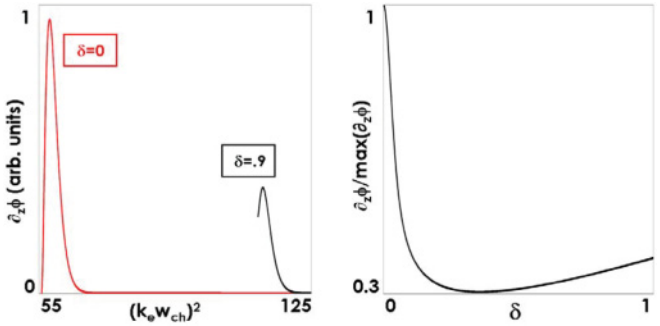

FIG. 12. (Color online) (a) Instability growth rates in the strong transverse phase-mixing regime as a function of plasma wavenumber in the axially uniform channel, red line (left) and modulated channel, black line (right). Cutoff in the growth rate is due to the resonance radius being imaginary. (b) Maximum growth rate as a function of modulation amplitude.

and modulation amplitude of $\delta = 0.9$. While the modulated wavenumber is larger, the growth rate is ~2.5 times smaller in the modulated channel. The cutoff in the $\delta = 0.9$ curve results from the condition $\hat{k}_e^2 > (1+\delta)k_{p,0}^2$. Figure 12(b) shows the maximum growth rate as a function of δ normalized to the $\delta = 0$ growth rate. The growth rate is lowered substantially even for small δ.

3. Finite pulse, no modulations

For determining the effect of pulse shape and duration on the growth rate, terms involving $\partial_\xi \hat{\phi}^*_{n,-}$ must be maintained. To demonstrate the effect of finite pulse shape, we will consider a Gaussian pulse shape of the form $\alpha(\xi) = \hat{\alpha}_0 \exp(-\xi^2/\sigma^2)$ and consider the case of coupled sidebands. Upon performing some algebra, we find that the evolution for the unstable Stokes sideband, including the pulse shape, is

$$\frac{\partial}{\partial z}\hat{\phi}_{n,\pm} = -i\frac{\pi}{2}\alpha_0^2(\xi)\left(\frac{\hat{k}_e}{\hat{k}_\pm}\right)[(\hat{k}_e - \partial_\xi\hat{\phi}^*_{n,-})w_{ch}]^2 P(r_*)\hat{k}_e, \tag{B7}$$

where $\hat{r}_* = \frac{1}{2}w_{ch}^2[(\hat{k}_e - \partial_\xi\hat{\phi}^*_{n,-})^2 - k_{p,0}^2]^{1/2}$. Equation (B7) is valid to lowest order in $O(k_p^{-1}\sigma^{-1})$, $O(w_{ch}^2/\sigma^2)$, and $O(k_p^{-2}w_{ch}^{-2})$, which for our parameters are ~0.007, ~0.003, and ~0.02, respectively. We note that Eq. (B7) is Eq. (B1b) including the pulse shape $\alpha^2(\xi)$, and with the complicated dependence on $\partial_\xi\hat{\phi}^*_{n,-}$. As it is difficult to obtain meaningful results by simplifying Eq. (B7) further, one must utilize simulations to examine the instability growth in this regime.

APPENDIX C: MAXIMUM GROWTH WITHIN A LASER PULSE

Equations (36a) and (36b) demonstrate that the exponentiation of perturbations within the laser pulse scale as

$$\mathrm{Im}[\omega t - kz] \propto z^a f^b(\xi), \tag{C1}$$

where a and b are rational numbers, and we remind the reader that $\xi = z - c_g t$. We want to find the time in the laser pulse for which the exponentiation is maximized. Differentiating Eq. (C1) with respect to z we have

$$\frac{\partial}{\partial z}z^a f^b(\xi) = az^{a-1}f^b(\xi) + bz^a f^{b-1}(\xi)\frac{\partial f}{\partial z}. \tag{C2}$$

Setting Eq. (C2) equal to zero and solving for z gives $z = -(a/b)(f/\partial_z f)$, and plugging back into Eq. (C1), we find that the maximum exponentiation occurs when

$$\mathrm{Im}[\omega t - kz] \propto \left[\frac{\partial f}{\partial z}\right]^b z^{a+b}. \tag{C3}$$

As an example we consider the situation where $a = b = \frac{1}{2}$ and $f = \xi$, and find that the maximum exponentiation occurs when $z = \frac{1}{2}c_{g0}t$.

APPENDIX D: CHANNEL WIDTH AND MODE WIDTH SCALING

Here we aim to find how the channel and mode width change with respect to one another. The widths of the mode profile and channel density scale as

$$L_m \equiv \left[\frac{1}{a}\frac{\partial a}{\partial r}\right]^{-1} \sim w_{ch}, \tag{D1}$$

$$L_{ch} \equiv \left[\frac{1}{\omega_p^2}\frac{\partial \omega_p^2}{\partial r}\right]^{-1} \sim (k_p w_{ch})^2 w_{ch}. \tag{D2}$$

The channel width decreases faster than the mode width as w_{ch} decreases. The variation of the mode across the channel width is then

$$\left|\frac{\Delta a}{a_0}\right| \sim (k_p w_{ch})^2 \exp[-(k_p w_{ch})^4], \tag{D3}$$

which decreases as w_{ch} increases. This is consistent with the growth rate increasing as channel width increases: the instability becomes increasingly less phase mixed.

[1] J. F. Drake, P. K. Kaw, Y. C. Lee, G. Schmidt, C. S. Liu, and M. N. Rosenbluth, Phys. Fluid **17**, 778 (1974).
[2] D. W. Forslund, J. M. Kindel, and E. L. Lindman, Phys. Fluids **18**, 1002 (1975).
[3] K. Mima and K. Nishikawa, J. Phys. Soc. Japan **38**, 1742 (1975).
[4] J. P. Palastro, E. A. Williams, D. E. Hinkel, L. Divol, and D. J. Strozzi, Phys. Plasmas **16**, 092304 (2009).
[5] E. Esarey, J. Krall, and P. Sprangle, Phys. Rev. Lett **72**, 2887 (1994).
[6] A. Ting, C. I. Moore, K. Krushelnick, C. Manka, E. Esarey, P. Sprangle, R. Hubbard, H. R. Burris, R. Fischer, and M. Baine, Phys. Plasmas **4**, 1889 (1997).
[7] S. P. LeBlanc, M. C. Downer, R. Wagner, S. Y. Chen, A. Maksimchuk, G. Mourou, and D. Umstadter, Phys. Rev. Lett. **77**, 5381 (1996).
[8] Z. Najmudin *et al.*, Phys. Plasmas **10**, 2071 (2003).
[9] C. Joshi, T. Tajima, J. M. Dawson, H. A. Baldis, and N. A. Ebrahim, Phys. Rev. Lett **47**, 1285 (1981).

[10] J. Krall, A. Ting, E. Esarey, and P. Sprangle, Phys. Rev. E **48**, 2157 (1993).
[11] E. Esarey, B. Hafizi, R. Hubbard, and A. Ting, Phys. Rev. Lett. **80**, 5552 (1998).
[12] T. M. Antonsen Jr. and P. Mora, Phys. Fluids B **5**, 1440 (1993).
[13] W. B. Mori, C. D. Decker, D. E. Hinkel, and T. Katsouleas, Phys. Rev. Lett. **72**, 1482 (1994).
[14] C. D. Decker, W. B. Mori, T. Katsouleas, and D. E. Hinkel, Phys. Plasmas **3**, 1360 (1996).
[15] N. E. Andreev, V. I. Kirsanov, L. M. Gorbunov, and A. S. Sakharov, IEEE Trans. Plasma Sci. **24**, 363 (1996).
[16] D. F. Gordon, B. Hafizi, P. Sprangle, R. F. Hubbard, J. R. Penano, and W. B. Mori, Phys. Rev. E **64**, 046404 (2001).
[17] C. G. Durfee III and H. M. Milchberg, Phys. Rev. Lett. **71**, 2409 (1993).
[18] H. M. Milchberg, C. G. Durfee III, and T. J. McIlrath, Phys. Rev. Lett. **75**, 2494 (1995).
[19] H. M. Milchberg, T. R. Clark, C. G. Durfee III, T. M. Antonsen Jr., and P. Mora, Phys. Plasmas **3**, 2149 (1996).
[20] G. Shvets and J. S. Wurtele, Phys. Rev. Lett. **73**, 3540 (1994).
[21] G. Shvets and X. Li, Phys. Plasmas **8**, 8 (2001).
[22] G. Shvets and X. Li, Phys. Plasmas **6**, 591 (1997).
[23] N. E. Andreev, L. M. Gorbunov, V. I. Kirsanov, K. Nakajima, and A. Ogata, Phys. Plasmas **4**, 1145 (1997).
[24] N. E. Andreev, and S. Y. Kalmykov, Plasma. Phys. Rep. **24**, 862 (1998).
[25] P. Sprangle, B. Hafizi, J. R. Penano, R. F. Hubbard, A. Ting, A. Zigler, and T. M. Antonsen, Phys. Rev. Lett. **85**, 5110 (2000).
[26] E. Esarey, C. B. Schroeder, B. A. Shadwick, J. S. Wurtele, and W. P. Leemans, Phys. Rev. Lett. **84**, 3081 (2000).
[27] S. Y. Kalmykov and G. Shvets, Phys. Plasmas **11**, 4686 (2004).
[28] V. Sajal, A. Panwar, and V. K. Tripathi, Phys. Scr. **74**, 484 (2006).
[29] E. J. Turano and C. J. McKinstrie, Phys. Plasmas **7**, 5096 (2000).
[30] V. Malka, J. Faure, J. R. Marques, F. Amiranoff, C. Courtois, Z. Najmudin, K. Krushelnick, M. R. Salvati, and A. E. Dangor, IEEE Trans. Plasma Sci. **28**, 1078 (2000).
[31] J. R. Penano, B. Hafizi, P. Sprangle, R. F. Hubbard, and A. Ting, Phys. Rev. E **66**, 036402 (2002).
[32] H. Figueroa and C. Joshi, in *Laser Interaction and Related Plasma Phenomena 7*, edited by H. Hora and G. Miley (Plenum Press, New York, 1986), p. 241.
[33] H. Figueroa and C. Joshi, Phys. Fluids **30**, 2294 (1987).
[34] C. Darrow, D. Umstadter, T. Katsouleas, W. B. Mori, C. E. Clayton, and C. Joshi, Phys. Rev. Lett. **56**, 2629 (1986).
[35] C. Darrow, W. B. Mori, T. Katsouleas, C. Joshi, D. Umstadter, and C. E. Clayton, IEEE Trans. Plasm Sci. **PS-15**, 107 (1987).
[36] B. D. Layer, A. York, T. M. Antonsen, S. Varma, Y.-H. Chen, and H. M. Milchberg, Phys. Rev. Lett. **99**, 035001 (2007).
[37] J. P. Palastro, T. M. Antonsen, S. Morshed, A. G. York, and H. M. Milchberg, Phys. Rev. E **77**, 036405 (2008).
[38] A. G. York, H. M. Milchberg, J. P. Palastro, and T. M. Antonsen, Phys. Rev. Lett. **100**, 195001 (2008).
[39] J. P. Palastro, and T. M. Antonsen, Phys. Rev. E **80**, 016409 (2009).
[40] T. M. Antonsen, J. P. Palastro, and H. M. Milchberg, Phys. Plasmas **14**, 033107 (2007).
[41] A. Bers, in *Handbook of Plasma Physics*, edited by M. N. Rosenbluth and R. Sagdeev, Vol. I, *Basic Plasma Physics*, edited by A. A. Galeev and R. N. Sudan (North-Holland, New York, 1983), p. 451.
[42] P. Mora and T. M. Antonsen Jr., Phys. Plasmas **4**, 217 (1997).
[43] P. Sprangle, J. Krall, and E. Esarey, Phys. Rev. Lett. **73**, 3544 (1994).
[44] T. M. Antonsen Jr. and P. Mora, Phys. Rev. Lett. **74**, 4440 (1995).
[45] G. Z. Sun, E. Ott, Y. C. Lee, and P. Gudzar, Phys. Fluids **30**, 526 (1987).